Chemistry Publications

Dept. of Chemistry

2015

Dynamic Control of Nanopore Wetting in Water and Saline Solutions under an Electric Field

D. Vanzo

D. Bratko
Virginia Commonwealth University, dbratko@vcu.edu

A. Luzar

Dynamic control of nanopore wetting in water and saline solutions under electric field

Davide Vanzo, Dusan Bratko[a,*], and Alenka Luzar[b,*]

Department of Chemistry, Virginia Commonwealth University,

Richmond, VA 23284-2006

Reversible, field-induced nanopore wetting by aqueous solutions, including electrolytes, provides opportunities for the design of hydrophobic valves for nanofluidics, control of surface-energy absorption in porous media and regulated wetting on corrugated surfaces. Conflicting porosity requirements have so far precluded direct implementations of fully reversible control: the pores have to be sufficiently wide to allow water infiltration at experimentally relevant voltages, but should not exceed the kinetic threshold for capillary expulsion in the absence of the field. As the activation barrier to water expulsion rapidly increases with the pore diameter, applicable widths are restricted below a few nanometers. Only a narrow window of fields and pore geometries can *simultaneously* satisfy both of the above requirements. Accurate accounts of wetting equilibria *and* dynamics at nanoscale porosity require molecular level descriptions. Here we use molecular dynamics simulations to study dynamic, field-controlled phase transitions between nanoconfined liquid and vapor phases in contact with unperturbed aqueous- or electrolyte-environment. In nanopores wetted by electrolyte solutions, we observe depletion of salt compared to the concentration in the bulk phase. The application of local electric field enhances the uptake of water and ions in the confinement. In systems prone to capillary evaporation, the process can be reversed at sufficient strength of the electric field. For alternating displacement field, we identify the conditions where O(ns) responses of the reversible wetting/expulsion cycle can be secured for experimentally realizable field strengths, porosity and salinity of the solution.

Keywords: nanoconfinement, electrolyte, graphane, constant chemical potential, electrostriction, molecular dynamics

a) dbratko@vcu.edu
b) aluzar@vcu.edu

I. INTRODUCTION

Reversible wetting of hydrophobic nano-channels or pores is of interest for a range of applications including hydrophobic nanofluidic valves[1,2], control of membrane permeability[3], energy storage in porous substrates[4-8], and regulated wettability of rough surfaces[9]. Affinity between the pore and water can be modulated by a variety of external stimuli, including light[2], temperature[10], pH[2], pressure[8,11,12] or electric field[1,2,12-22]. Because of comparative ease of application, and fast and uniform control, several experimental studies[1,2] examined the use of applied field in *dynamic* wetting experiments. Together with related studies concerned with capillary condensation[19,23,24], these works show wetting of hydrophobic nanopores could generally be induced by the field. However, at *above* a few nm porosity, reversible dewetting of pores surrounded by an aqueous bath presents a challenge, with wetted state kinetically stalled[2] because of high activation barriers for evaporation[25-33]. Reversibility was therefore secured through the retention of localized air or vapor bubbles, which acted as nucleation centers for subsequent evaporation[1,2]. Pockets of gas were preserved by preventing complete water intrusion[2], or by adsorption of gas at hydrophobic patches on chemically patterned walls[1].

Descending to even narrower $O(1)$ nm pores, in this work we demonstrate the possibility of *complete*, fully reversible wetting/dewetting transitions by using molecular dynamics (MD) simulations. Molecular approach is essential as aqueous nano-confinements show important quantitative and qualitative deviations from the continuum picture[34,35], both in the absence[26,28,30,36-41] and presence[13,16-18,21,22,42-44] of applied electric field. Main differences can be explained in terms of interfacial hydrogen bonding[45-48], responsible for anisotropic polarizability of aqueous interfaces and associated field-direction effects[18,21,44,48,49]. In short, the lateral component of the permittivity tensor in a nanoscale slit is about twice bigger than the normal one. Likewise, the field-induced increase in surface wettability is notably stronger in a parallel than normal field. When the field is applied across the pore, a Janus interface can emerge, with wetting propensity at the wall under incoming field exceeding the one in the outgoing field[18,44,48]. Anisotropy in polarization *dynamics* of interfacial water revealed in recent MD simulations[50] can be even more pronounced than for static properties. These effects are negligible at the macroscopic level but can modulate the phase behavior in nanoscale systems, characterized by strong representation of surface molecules.

Below, we describe the first simulation study of dynamic, field-controlled phase transitions in nanoconfined water. Because of potential role dissolved ions *could* play in these electrostatically driven processes[14,51,52], and their relevance in nanofluidics applications, we consider both the neat water and electrolyte solutions. As described in Model and Methods section, our approach builds on the methodology we developed in a recent study of equilibrated, fully wetted pores under static electric field[53]. The pore is immersed in an unperturbed bath at constant peripheral pressure and fixed chemical potential. We describe a generalization to uniformly varying fields across the confinement. We monitor the system evolution upon abruptly or gradually changing the displacement field in the nanopore to induce water infiltration or expulsion. To suppress the barrier to dewetting, we use very narrow pores, which in turn require stronger electric fields to trigger infiltration. Continuum electrostatics offers rough estimates of threshold electric displacement field, D_z, while we deduce the profile of the electric field E_z, modulated by dielectric screening, from the simulation results. Insights into filling/expulsion equilibria in confinements *surrounded by liquid bath*, obtained in our study, are readily applicable to the reverse problem of capillary condensation from, and evaporation to the surrounding vapor phase[19,23,24]. A separate study would, however, be needed to characterize the distinct transition kinetics in the latter scenario.

In Results section we compare temporal profiles of the liquid density inside the nanopores for different increasing or decreasing field rates. For O(nm) wide apolar pores, complete wetting-dewetting cycles can be repeated with no restrictions. We observe only small variations of the *infiltration* (forward) branches in individual cycles. Insignificant influence of the rate of the field increase implies small or negligible barriers to liquid *intrusion*. The reverse branch, on the other hand, is poorly reproducible. A pronounced hysteresis and large variance of expulsion times are indicative of a notable barrier to expulsion. In view of rapid increase of the barrier with inter-wall separation[25,27,29-33], spontaneous expulsion only takes place at pore widths below a few nm. In salt solutions narrow widths are conducive to salt depletion. We can then expect the applied field to partially offset this effect. Our simulations show ions entering to, and withdrawing from, the pore together with surrounding water, however, the salt molality is generally lowered inside the confinement. In uncharged nanosized pores we consider, the presence of salt does not alter the occurrence, or rate, of the observed phase transitions in any significant way. This observation is indicative of a comparatively weak role of electro-osmotic

flow[14] effects. For specified pore and field parameters, it hence supports generalizations of model predictions for nanopore gating to include pure water as well as ionic solutions.

II. MODEL AND METHODS

A. Simulated system

To capture transport processes between field-exposed confined phase and unperturbed solution, a small model pore is embedded in a bigger field-free reservoir (Fig. 1). The temperature is held at 300 K using Nose-Hoover thermostat[54]. Constant pressure in the bath, close to vapor pressure of water, is maintained by pressure-buffering[22,55,56], provided by coexisting liquid and vapor domains. For this purpose, two vapor pockets are created in the regions adjacent to purely repulsive walls, placed at the top and bottom boundaries of the rectangular simulation box, as illustrated in Fig. 1. Water molecules interact with the repulsive walls through a harmonic potential with spring constant of 84 kJ mol Å^{-2}. A detailed description of the method is given in the preceding work[22]. The box accommodates 8282 water molecules, along with N_{NaCl}=153 ion pairs when modeling 1.027 mol kg^{-1} salt solution.

For easier comparisons with previous studies[12,13,16-18,22,43,44,57-60] we represent water molecules using the extended simple point charge model (SPC/E)[61]. The model has repeatedly been shown to provide satisfactory descriptions of dielectric and interfacial properties[62-67] of liquid water, an essential requirement for our study. In analogy to other classical-simulation models of water, SPC/E model does not capture water dissociation. In simulated systems of size of up to 10^4 water molecules, this ignores the rare presence of dissociated ion pairs: at neutral pH a single pair of ions would on the average be present in the simulated system over about 0.01% of the time of observation. While strong electric fields can enhance dissociation of water in microchannels[68], our calculations at Na$^+$ and Cl$^-$ concentrations as high as 1 mol kg^{-1} reveal at most a minute influence of dissolved ions on the occurrence *and* rate of field-controlled nanopore wetting and expulsion, the central phenomena of the present study.

In the center of the box, we place a nanopore comprised of a pair of parallel platelets of circular shape. This geometry minimizes the area of the liquid-vapor interface formed in case of capillary evaporation from the pore, and enables a symmetric decay of electric field applied across the confinement. To enable spontaneous expulsion of water in the absence of the field, the

nanopore walls are made strongly hydrophobic materials, devoid of polar or ionizing groups. This way, the confinement can switch from strongly hydrophobic in the absence of the applied field to hydrophilic in its presence. While enabling wettability control over a broad range, nonpolar materials we use are not intended to mimic conditions in nanoporous membranes, where polar moieties and even charges are commonplace. Our model pore walls are carved from a plate of butyl-functionalized[69] graphane[70,71], a hydrogenated form of graphene with high band gap[72] and planar structure insensitive to chemical substitutions. The insulating properties of graphane make it a suitable prototypical material for simulations in the presence of ions or externally applied field. In a previous work, we determined the contact angle of water on pure graphane at ~73°. Functionalization by butyl groups with surface density of 4.01 nm^{-2}, a typical density of physisorbed SAMs layers, brings the contact angle to that of a hydrocarbon[69]. To improve computational efficiency, in this work, graphane is modeled using the united-atom representation with hydrocarbon groups described as Lennard-Jones entities with interaction parameters we collect in Table I. These parameters are based on OPLS-UA force fields with energy constant ε of the terminal –CH$_3$ group parameterized to capture the target contact angle of a strongly hydrophobic hydrocarbon brush. We used Na$^+$ and Cl$^-$ force fields of Fyta and Netz[73]. The ion force fields were parameterized with Lennard-Jones cutoff of 9 Å, hence we adopted this cutoff for all Lennard-Jones interactions. Lorentz-Berthelot mixing rules are used to describe water-ion, water-surface, and ion-surface interactions.

The pore wall diameters were 34 Å or 64 Å, with interplate separation measured between graphane plates at 23 Å or 31 Å, respectively. Corresponding separations between terminal methyl groups at opposing plates were ~11 Å or 19 Å. The thickness d of the confined aqueous slab accommodated inside the pore at these separations (measured from the positions of the Gibbs dividing surfaces) was 7 or 15 Å (See Fig. 2). The bath water layers above and beneath the confinement spanned around 2-2.5 nm, a thickness proven sufficient to avoid evaporation events within these layers. The 7-10 Å wide vapor pockets acting as pressure buffer[64,22,56] occupied the space between the aqueous slab and the upper or bottom wall of the simulation box. The resulting system is self-barostating in *NVT* ensemble, with vanishing normal component of reservoir pressure. The lateral pressure components are negative consistent with the positive interfacial free energy at the vapor-liquid interface.

Long-range interactions were treated by particle-particle-particle mesh solver (PPPM)

with a real space cutoff of 9 Å and relative precision tolerance in force per atom of 10^{-5}. The Yeh-Berkowitz correction to the Ewald summation[74] was used to account for the two-dimensional periodicity of our system.

B. Contact angle measurement

Reversible wetting and expulsion of water or solution from nanopores requires a careful selection of system properties. Within a continuum approximation, the widths supporting spontaneous water expulsion from a cylindrical pore of diameter $2R$ can be estimated by a modified Kelvin equation for planar confinements of finite lateral size[26]

$$d \leq -\frac{2\Delta\gamma}{P + 2\gamma R^{-1}} \qquad (1)$$

Here, d is the thickness of water slab in the pore, P is external pressure, γ is surface tension of the liquid and $\Delta\gamma = -\gamma \cos\theta_c$ the wetting free energy of the pore walls. Information about the wall contact angle θ_c is therefore important for the design of the system. We determined the contact angle of water on our functionalized surface from the simulations of *cylindrical* nanodroplets as described in a former work[75]. A 6600 molecules nanodrop was placed on a rectangular graphane sheet of dimensions 12.4x19.1nm^2 and the contact angle sampled over several nanoseconds following ~0.1 ns equilibration. Cylindrical drop geometry essentially eliminated line tension effects, providing a good approximation to contact angles converged with respect to droplet's size. For model parameters from Table 1, with ε_{CH3}=0.1 kcal mol^{-1} and short-range interaction cutoff of 9 Å, contact angle was 128±3°. To explore the possibility of the contact angle reduction due to the presence of water surrounding the pore, we repeated contact angle calculations on graphane substrate sitting on ~ 1.6 nm thick aqueous slab. A statistically insignificant average reduction by 1-2° was found in the presence of the slab. The lack of 'wetting transparency' [76,77], observed in contact angle measurements on graphene, is explained by the notably greater thickness of the butylated graphane used in our system. We report on measurable contact angle changes due to the presence of water under graphene in a separate work[78].

For nanoscale pore *diameters R*, and ambient pressure P, the denominator in Eq. (4) is dominated by the surface tension term, which reflects the cost of forming the liquid-vapor interface at the pore perimeter. The inequality $\gamma R^{-1} >> P$ leads to a simpler thermodynamic

condition for evaporation, $d < -R\cos\theta_c$. For our smaller pore size, $R\sim17$Å, this suggests d should be held below ~11Å, corresponding to the distance between terminal methyl groups on distinct walls $h\sim15$Å (separation between graphane plates ~27Å). We choose h at 11Å and $d\sim7$Å. As d measures the width available to the centers of water oxygens, the pore accommodates about three layers of water molecules. To observe capillary evaporation in wider pores will generally require increasing the lateral dimension of the pore, R. However, while increased R eases the thermodynamic condition for evaporation given by Eq. (4), liquid can still remain stalled in the pore kinetically. Kinetic barrier to evaporation is known to rapidly increase with the width of the pore. In hydrocarbon nanopores, the barrier becomes prohibitive beyond a few nm width, with metastable liquid persisting over all practically relevant times[25,29-33] even for macroscopic lateral size R.

C. Electric field

To mimic the conditions between extended hydrophobic walls under a homogeneous field, a uniform electric displacement field $D_z(r) = D_z(0)$, perpendicular to pore walls, is imposed across the core of the cylindrical confinement at distances from the central axis $r < r_{in}$ (Fig. 1). The field $\boldsymbol{D}(r)$ describes the contribution of (implicit) external charges[22] to the local electrostatic potential, $\psi(r,z)$. ε_0 is the permittivity of vacuum and D_z can be viewed as surface density of the charge stored in a capacitor. The force acting on a molecular or ion charge q_i due to the imposed field is therefore $\boldsymbol{F}_i = q_i\boldsymbol{D}(r)/4\pi\varepsilon_o$. To avoid the complications associated with the MD integration in a discontinuous field[22], at distances exceeding r_{in}, the field D_z gradually decays over a finite interval $r_{in} \le r \le r_{out}$, vanishing at the confinement border, $r=r_{out}$. The field decay with r is described by the relation

$$D_z(\text{r}) = D_z(0)\ g(\text{r})\ \text{ with}$$

$$(2)$$

$$g(r) = \begin{cases} 1 & \text{for } r_s \leq 0 \\ \frac{1}{2}[\cos(\pi r_s) + 1] & \text{if } 0 \leq r_s \leq 1, \; r_s = \dfrac{r - r_{in}}{r_{out} - r_{in}} \\ 0 & \text{for } r_s > 1 \end{cases}$$

The radial electric displacement field component, $D_r(r,z)$, vanishes in homogeneous regions ($r < r_{in}$ or $r > r_{out}$), but is nonzero within the region of varying, $D_z(r)$, $r_{in} \leq r \leq r_{out}$. Since $\mathbf{D}(r,z)$ is a conservative vector field,

$$\frac{\partial^2 \psi(r,z)}{\partial z \partial r} = \frac{\partial^2 \psi(r,z)}{\partial r \partial z} \quad , \; i.e. \quad \frac{\partial D_r(r,z)}{\partial z} = \frac{\partial D_z(r,z)}{\partial r} \tag{3}$$

For the specific form of $D_z(r)$, Eq. (1), and the symmetry condition $D_r(r,0) = 0$, integration of Eq. (3) gives

$$D_r(r,z) = z D_z(0) \frac{\partial g(r)}{\partial r} \tag{4}$$

The details of the method, and its advantages over the use of explicit wall charges, are described in ref.[22]. The smooth variation of the field supports the use of standard MD. Our computations were performed using the LAMMPS simulation package with the Velocity Verlet integrator and simulation time step 1 fs. Stability of the integrator and the pressure-buffering method were verified in test *NVE* simulations as described in previous work[22].

To drive the liquid into a hydrophobic pore, Maxwell stress[14,19,79,80] has to overcome the Laplace pressure associated with unfavorable wetting free energy of the pore. For a pore with finite diameter ($2R$) under a uniform electric displacement field $\mathbf{D} = (D_z, 0, 0)$, a 1st order continuum-estimate for the thermodynamic condition for infiltration, analogous to Eq. (1), takes the form[21,81]

$$d \geq \frac{2\Delta\gamma}{P + \dfrac{D_z^2}{2\varepsilon_o}\left(1 - \dfrac{1}{\varepsilon_r}\right) + \dfrac{2\gamma}{R}} \tag{5}$$

where ε_r approximates the relative permittivity of confined liquid inside a wetted pore. We underscore that the mean-field estimates (eqs. 5-7), relying on continuum concepts, serve merely

for a ballpark assessment of field effects. More rigorous continuum level analyses of static properties *and* transition dynamics are possible following refs.[14,52] but are outside the scope of our molecular level study. For O(nm) pore diameters, ambient pressure P can be neglected in comparison to the surface tension term in the denominator. For fixed separation d, and $\varepsilon_r^{-1} \ll 1$, Eq. (5) can be rewritten as a condition for minimal displacement field capable of triggering infiltration into the pore,

$$D_z \geq \sqrt{-4\gamma\varepsilon_o(\cos\theta_c d^{-1} + R^{-1})} \qquad (6)$$

For present pore dimensions, R=17Å, d=7Å, and $\gamma_{SPC/E} \sim 0.0633$ Nm^{-1} [82], $\theta \sim 128°$, the above relation suggests the threshold electric displacement field strength $D_z \sim 0.026$ Cm^{-2}. To explore the possibility of field-induced infiltration in our hydrophobic pore, we consider a window of simulated electric displacement fields from zero to ~ 0.03 Cm^{-2}. Reductions of the necessary strength of the field are possible by increasing wall-wall separations. Two or even three-fold increase of d could be kinetically viable, however, the concomitant increase of evaporation times renders these situations less suitable for MD simulation studies.

In the presence of water, the actual electric field $\boldsymbol{E}$ is well below $\boldsymbol{D}/\varepsilon_o$ due to dielectric screening. In an isotropic aqueous phase, $\boldsymbol{E}=\boldsymbol{D}/\varepsilon_o\varepsilon_r$, however, this relation is inaccurate in a nanoconfinement where both $E_z(z)$ and (tensorial) relative permittivity show complex dependences on the distance from the confinement walls[83,84]. Following previous work[22], we obtain the first order estimate for the actual electric field inside the pore from local orientational polarization of water molecules. Average cosine of the angle between water dipoles and the direction of the field, θ_z, has been shown to provide a good measure of the field strength inside a field-exposed confinement[85]. In a recent study, we have shown[22] how the *change* of $<\cos\theta_z>$ can inform us about the local field in systems with preexisting interfacial polarization[50] observed even in the absence of external field. The reader is referred to ref.[22] for details about the method and the calibration of $\Delta<\cos\theta>$ *vs* E_z for the present model[61] of water. Panels (a) and (b) in Fig. 3 illustrate spontaneous orientation of water dipoles inside the nanopore between a pair of butylated graphane disks with radius r_{out}=17Å at (methyl-methyl) separation h=11Å at zero field (a) and at D_z=0.031 Cm^{-2}, the strongest displacement field we consider (b). Panel (c) illustrates the estimated profile of the total field strength normal to the confinement walls, $E_z(z)$. For the

specified displacement field D_z, the field strength inside the aqueous slab ($|z| \leq \sim 4\text{Å}$) is shown to vary between $\sim (1 - 2) \cdot 10^{-2}$ VÅ^{-1}, hence the total voltage across the slab is of $O(10^{-1})$V. According to these results, the mean of the inverse normal component of the relative permittivity inside the confined aqueous slab, $<\varepsilon_{zz}^{-1}>$, is between 20^{-1} and 30^{-1}. Fields of comparable strength can be routinely generated next to an AFM tip[86]. Using appropriate electrode insulation, μm aqueous films inside a capacitor at stationary field $E \sim 0.013$ VÅ^{-1} have been found stable over arbitrarily long times of observation[87]. $O(10^{-2})$ VÅ^{-1} fields barely exceed the linear regime of orientational polarization[22,88]. Based on experimental polarizability of water molecule $\alpha \sim 1.5\text{Å}^3$, these fields are too weak to induce a noticeable (>0.25%) change of molecular dipole in the liquid phase, and definitively well below the decomposition threshold field of ~ 0.3 VÅ^{-1} [89,90].

III. RESULTS AND DISCUSSION

A. Pure water

Abrupt imposition, or cessation of external field

For selected nanopore dimensions and ambient conditions ($P \sim 0$, $T = 300$ K), equilibration results in empty confinement regardless of initial configuration. The left panel of Fig. 4 illustrates the uptake of water that follows the imposition of displacement field of strength 0.031 C m^{-2} (field corresponding to capacitor electrode charge density of approximately an elementary charge per 6-7 nm^2). The initial, evacuated state is equilibrated in the absence of the field. While much of the pore in this state is empty, the number of confined (axial distance $r < r_{out}$) molecules, N_{H2O}, fluctuates around 5-7% of the number observed in a fully wetted pore, an effect attributed to the convex shape of the liquid/vapor interface at the pore boundary.

The process of infiltration begins the moment the field is turned on and, for given geometry, completes in $\sim 0.2 \pm 0.05$ ns. The rate of infiltration appears faster in the initial stage that corresponds to the adjustment in the meniscus curvature at the liquid/vapor interface in response to the attraction of water into the region under the field. The plots for three independent runs, illustrated in Fig. 4, indicate about 25% of the pore volume is filled at this stage. The process proceeds at a somewhat slower pace as further infiltration involves unfavorable wetting of pore walls. The final stage corresponds to the collapse of the vapor bubble in the center of the

pore.

When the field is turned off (time t=1.25 ns in Fig. 4), we observe an immediate 17-19% decrease in water density inside the pore. The magnitude of this change is compatible with the reversal of electrostriction of the confined liquid phase, consistently observed upon imposition of similar fields in preceding works[16,18,22,43]. Once electrostriction is lost, water density fluctuates around the density of metastable liquid until a sufficient thermal fluctuation brings the system across the free energy barrier to cavitation. As the evaporation process depends on rare fluctuation events, the times of evaporation observed in multiple intrusion/expulsion cycles are scattered over a broad range from below 0.4 to several ns. Only about 0.1 ns elapses from the time of ~15% depletion and complete evacuation. In many runs beginning in fully wetted state and the field turned off, not a single system has recovered its initial density after >15% depletion, suggesting the radius of the critical vapor nucleus R^* around 6-7Å. A mean field approximation for the barrier to vapor nucleation can be obtained by considering the surface free energy of a cylindrical bubble[25,31] of radius r, $\Delta\Omega(r)\sim2\pi rd\gamma+2\pi r^2\gamma\cos\theta_c+P\pi r^2d$, with the maximum at $r=r^*\sim5.7$Å The estimated nucleus radius is in reasonable agreement with the apparent size of 6-7Å deduced from the simulation. The mean field estimate for the barrier itself, $\Delta\Omega^*(r^*)\sim7.9\cdot10^{-19}$J or ~19 k_BT is less reliable, exceeding more accurate umbrella sampling results for similar systems[29-31,33]. Applying umbrella sampling Monte Carlo, we determined[31] the evaporation barrier in a laterally extended pore of width h=14Å, $d\sim10$Å, and θ_c=135° at 18.7±1 k_BT. According to the known scaling relation $\Delta\Omega^*\propto d^2/\cos\theta_c$ [25,32], extrapolation to d=7Å, θ_c=128° obtains $\Delta\Omega^*\sim10.4$ k_BT, a value in reasonable agreement with observed evaporation kinetics. Using the observed evaporation times τ_e of $O(0.1\text{-}10)$ ns, and the crude relation $\tau_e\sim(2\pi\hbar/k_BT)\exp(\Delta\Omega^*/k_BT)$ suggests activation barriers between 7-11 k_BT (k_B and $2\pi\hbar$ denote Boltzmann and Planck constants).

Uniformly varying field

Response times observed in the above example suggest $O(10^{-1})$ GHz is the limiting field frequency the system would be able to follow. To explore the temporal response further, and to identify the threshold field amplitude for pore wetting, we monitored the infiltration and expulsion processes under uniformly increasing or decreasing displacement fields. We compare results for two rates of field change, $dD_z/dt = \pm\ 9\cdot10^{-3}$ Cm^{-2} ns^{-1} or $\pm\ 4.5\cdot10^{-3}$ Cm^{-2}ns^{-1}. Fig. 5

describes a typical cycle in terms of the dependence of the number of confined water molecules, N_{H2O}, as a function of D_z for the bigger rate of $\pm 9 \cdot 10^{-3}$ Cm^{-2} ns^{-1}. The weak initial response at fields below $\sim 2 \cdot 10^{-2}$ Cm^{-2} can be attributed to the change in the meniscus curvature discussed with Fig. 4, while the rapid increase in N_{H2O} between $(2.2\text{-}2.5) \cdot 10^{-2}$ Cm^{-2} reflects full scale infiltration, which entails wetting of confinement walls. The threshold displacement field is surprisingly close to the continuum estimate of $\sim 2.5 \cdot 10^{-2}$ Cm^{-2} provided by Eq. 5 (see text below this equation). The gradual density rise beyond the infiltration transition is consistent with intensified electrostriction in a fully wetted nanopore.

The backward (expulsion) branch in the window of strong fields, where the pore is filled by the liquid, reflects the reduction in N_{H2O} due to a gradual reversal of electrostriction with weakening the field. In this regime, the backward branch coincides with the forward one. When the field is decreased below the threshold strength for infiltration, however, the liquid typically persists in the pore. The expulsion is delayed until the field strength falls much lower, generally below 10^{-2} Cm^{-2}. In a fraction of runs, the field actually vanished before the evaporation took place. The pronounced hysteresis is explained by the activation barrier to expulsion, associated with the creation of the interface between the liquid and vapor phases. Conversely, the infiltration process begins with liquid/vapor interface already in place and the area of the interface decreases as the pore is filled with water. The barrier to evaporation is expected to further increase in the presence of applied field, as the field stabilizes fully wetted states in comparison the partially evacuated ones. As will be shown shortly, this expectation is borne out in trial calculations where we switch from forward to backward branch before complete infiltration.

First, however, we survey a set of complete cycles where the field change was reversed after *complete* filling of the pores. Fig. 6 summarizes the results of five cycles completed at the field change rate $dD_z/dt = \pm 9 \cdot 10^{-3}$ Cm^{-2} ns^{-1}, along with additional three cycles at twice smaller rate of $\pm 4.5 \cdot 10^{-3}$ Cm^{-2}ns^{-1}. The three cycles shown in different colors correspond to the higher rate. In one of them, evaporation took place after the field fell to zero. Regardless of the rate of field decay, evaporation was never observed at the displacement field above 0.01 Cm^{-2}, which is below one half of the threshold for infiltration. Wide scatter of evaporation events below this

field reflects the rare event character of the process, rather than its reliance on further weakening of the field. The infiltration branches are more reproducible. All of the remaining 6 cycles fell within the range of the three infiltration curves shown in Fig. 6. Three of these six cycles were performed at twice slower field change, $dD_z/dt = \pm\ 4.5 \cdot 10^{-3}$ Cm^{-2}ns^{-1}, yet we observe no systematic deviation from the results obtained at the higher rate. The only significant difference between individual cycles was found in times, and associated field strengths, corresponding to abrupt evaporation events. We identify these events by registering positions of 50% evacuation. In Fig. 6, they are marked by solid circles (higher field change rate) or triangles (slower rate). Interestingly, all evaporation events observed at the slower rate are grouped within the displacement field interval between D_z=0.5-1.0$\cdot$10^{-2} Cm^{-2}. This observation confirms that rarity in time is the primary cause of poor reproducibility of the backward (evacuation) branch. By and large evaporation times of 10 ns suffice for complete evacuation of water from the nanopore even when the field is turned off smoothly rather than in a stepwise fashion.

Electrolyte solution

So far, we have considered only pure water. Dissolved ions could, however, be present in many applications, ranging from nanofluidics to controlled permeation of porous electrode materials. In addition to electrostatic shielding, ions can modulate field effects on nanopore wetting by supporting electro-osmotic flow in the channels[14]. These possibilities are examined by extending our model calculations to a few cases where pure water is replaced by NaCl solutions. We used a relatively high bulk molality of 1.027 mol kg^{-1} to amplify any changes. Molality was chosen to quantify the salt content as it represents an unambiguous measure of concentration under confinement conditions. In view of reduced opportunities for ion hydration, salt concentration in a hydrophobic confinement is lower than in the surrounding bath. Because of poor statistics attainable in molality calculations in our 7Å wide confinement, in Fig. 7 we illustrate the qualitative trend by comparing confined and bulk NaCl molalities in bigger pores made up of identical wall material but with diameter 64Å, r_{out}=32Å and d=15Å, for three values of r_{in}, 24, 16, or 8Å and the displacement field D_z=0.031 Cm^{-2}. Despite attraction by the field, the interior ion concentration remains at about 70±5% of the bulk one. For the smallest core volume, r_{in}=8Å, only a handful of ions are present and we observe frequent deviations from local neutrality with slight preference for Cl- ions. The trend toward salt depletion intensifies in the

narrow slit with $d = 7$ Å. Here, ions with intact first hydration shell are limited to a thin layer $|z| \leq$ 1Å from the midplane of the pore. The remaining core molality of the ions shows big fluctuations around the average value of O(0.1) mol kg-1 with strong dominance of sodium ions. Small number of confined ions (mostly 0 or 1) precludes accurate statistics of ion molalities in these pores.

Fig. 8 illustrates several wetting/dewetting cycles analogous to those shown in Fig. 6, except that the liquid was 1.027 mol kg^{-1} NaCl solution. The rate of field change $dD_z/dt = \pm$ $9 \cdot 10^{-3}$ Cm^{-2}ns^{-1}. While not explicitly measured, any contribution of electro-osmotic flow is implicitly captured in the simulation in the presence of salt ions. Within the noise associated with thermal fluctuations, the curves obtained in the presence of the salt are hardly distinguishable from those shown in Figs. 5-6 for pure water. Likewise, the simulated infiltration under the slowly changing field, $dD_z/dt = \pm 4.5 \cdot 10^{-3}$ Cm^{-2}ns^{-1} (Fig. 9), reveals no change compared to the faster process shown in Fig. 8. The small increase in saline contact angle, compared to that of pure water[58], shifts the infiltration transition to a slightly stronger displacement field. This change is consistent with salt-induced increase of infiltration pressure observed[8] in wider nanopores. While the addition of salt has shown a moderate hysteresis reduction of the infiltration-expulsion cycle under pressure control[7,8], no statistically meaningful trend could be deduced from our simulation results. Notwithstanding small quantitative adjustments, the above comparisons indicate our findings obtained in pure water simulations also apply to salt solutions, at least for selected conditions.

Incomplete cycles

To estimate the position of the activation barrier to water expulsion in the presence of the field, in a number of runs started under uniformly increasing D_z we initiate the reverse process (field decrease) from incompletely filled configurations. As illustrated by the examples presented in Fig. 10, if the infiltration already reached ~65-70% completion, it promptly proceeded toward the fully filled state even under *decreasing* field. These result indicates the likely radius of the critical vapor nucleus, $r^*(D_z)$, corresponding to the activation barrier for evaporation at the specified field strength ($D_z \sim 0.025$ Cm^{-2}) to be around 8.5±1Å. This value is comparable to the mean field prediction. In analogy with our earlier estimate of the nucleus size in the absence of the field (Section III.A), one can approximate free energy of cavitation as a function of the radius

of cylindrical vapor cavity in the pore center for finite D_z[16],

$$\Delta\Omega(r,D_z) \sim 2\pi r d\gamma + 2\pi r^2 \gamma \cos\theta_c + \left[P + \frac{D_z^2}{2\varepsilon_o}(1 - \frac{1}{\varepsilon_r}) \right]\pi r^2 d \qquad (7)$$

At D_z~0.025 Cm^{-2}, $\Delta\Omega(r,D_z)$ passes through maximum at r^*~8.3 Å. If the field begins decreasing *before* the vapor cavity shrunk below the critical size r^*, infiltration is reversed without delay. However, once the cavity collapses, because of Maxwell stress contribution (the last term in Eq. 7), the barrier to vapor nucleation remains prohibitive (upper-bound mean field estimate $\Delta\Omega(r^*,D_z)$~27 $k_B T$), delaying eventual expulsion until D_z is significantly reduced. In our simulations, expulsion occurred only at displacement fields below ~0.01 Cm^{-2}. The same applied to 1 mol kg^{-1} NaCl solution, and we observe no significant effect of added salt on the hysteresis of the wetting-dewetting cycle.

While we focused on a single pore size because of computational constraints, extrapolations to other sizes are possible based on our results and fair agreement with mean field relations, Eqs. (1), (5) and (6). According to Eq. (5), increasing the pore diameter d will reduce the magnitude of displacement field required for infiltration. Because of steep rise of activation barrier[29,32] to expulsion with d, in case of water, the increase in d is limited to below ten molecular diameters[25,26,30,31,33]. Combining the effect of the field *and* external pressure, on the other hand, can facilitate intrusion when the pores prove too narrow to be wetted under electric field alone[12]. Based on Eq. 6, electric control of nanopore filling can be extended to other nonwetting liquids provided the inverse dielectric constant, ε_r^{-1}, is sufficiently different from unity, a condition fulfilled by strongly *and* moderately polar liquids.

Concluding remarks

Our molecular simulations show applied electric field can enable *reversible* control of wetting and dewetting in hydrophobic nanopores. In similar experimental and theoretical studies, reversal of filling transition relied on the remnants of air or vapor inside the wetted pores. In narrow carbon nanotube pores conducive to spontaneous evaporation, on the other hand, infiltration required increased pressure in addition to the field[12]. Using appropriate pore geometry, we observe complete phase transitions inside the confinement, controlled solely by the applied field.

Fair estimates of critical pore dimensions and required external field, as well as the dimensions of the vapor nuclei associated with the kinetic barrier to water expulsion, can be obtained from a continuum/mean field picture. Neglecting crucial thermal fluctuations, this approach is adequate to predict qualitative trends, but overestimates absolute magnitudes of activation barriers. In ~ 1 nm sized pores, kinetic barriers result in pronounced wetting-dewetting hysteresis, yet they cannot support long-lived metastable confined liquid phases unless assisted by at least of a fraction of the field initially required for infiltration. Our observations in neat water remain essentially unchanged in the presence of salt ions, suggesting any electro-osmotic effect to be weak at the specific conditions. The addition of salt slightly increases the threshold field for infiltration but does not appear to alleviate the hysteresis, as indicated in earlier measurements. Our studies set the stage for the design of field-controlled nanofluidic valves, regulated pore permeation, absorption of surface energy in a hydrophobic porous medium, and nanofluidic transistors[91] driven by electrically stimulated phase transitions.

(1)   Powell, M. R.; Cleary, L.; Davenport, M.; Shea, K. J.; Siwy, Z. S. *Nature Nanotechnol.* **2011**, *6*, 798-802.

(2)   Smirnov, S. N.; Vlassiouk, I. V.; Lavrik, N. V. *ACS Nano* **2011**, *5*, 7453-7461.

(3)   Lifton, V. A.; Taylor, J. A.; Vyas, B.; Kolodner, P.; Cirelli, R.; Basavanhally, N.; Papazian, A.; Frahm, R.; Simon, S.; Krupenkin, T. *Applied Physics Letters* **2008**, *93*, 043112.

(4)   Eroshenko, V.; Regis, R. C.; Soulard, M.; Patarin, J. *J. Am. Chem. Soc.* **2001**, *123*, 8129-8130.

(5)   Eroshenko, V.; Regis, R. C.; Soulard, M.; Patarin, J. *Comptes Rendus Physique* **2002**, *3*, 111-119.

(6)   Soulard, M.; Patarin, J.; Eroshenko, V.; Regis, R. In *Recent Advances in the Science and Technology of Zeolites and Related Materials, Pts. A-C* 2004; Vol. 154, p 1830-1837.

(7)   Kong, X. G.; Surani, F. B.; Qiao, Y. *Phys. Scr.* **2006**, *74*, 531-534.

(8)   Kong, X.; Qiao, Y. *Applied Physics Letters* **2005**, *86*, 151919.

(9)   Krupenkin, T.; Taylor, J. A.; Kolodner, P.; Hodes, M. *Bell Labs Technical Journal* **2005**, *10*, 161-170.

(10)   Krupenkin, T. N.; Taylor, J. A.; Wang, E. N.; Kolodner, P.; Hodes, M.; Salamon, T. R. *Langmuir* **2007**, *23*, 9128-9133.

(11)   Smirnov, S.; Vlassiouk, I.; Takmakov, P.; Rios, F. *Acs Nano* **2010**, *4*, 5069-5075.

(12)   Xu, B. X.; Qiao, Y.; Zhou, Q. L.; Chen, X. *Langmuir* **2011**, *27*, 6349-6357.

(13)   Vaitheeswaran, S.; Rasaiah, J. C.; Hummer, G. *J. Chem. Phys.* **2004**, *121*, 7955-7965.

(14)   Takhistov, P.; Indeikina, A.; Chang, H. C. *Physics of Fluids* **2002**, *14*, 1-14.

(15)   Liu, J.; Wang, M. R.; Chen, S.; Robbins, M. O. *Phys. Rev. Lett.* **2012**, *108*, 216101.

(16)   Dzubiella, J.; Hansen, J. P. *J. Chem. Phys.* **2005**, *122*, 234706.

(17)   Vaitheeswaran, S.; Yin, H.; Rasaiah, J. C. *J. Phys. Chem. B* **2005**, *109*, 6629-6635.

(18)   Bratko, D.; Daub, C. D.; Leung, K.; Luzar, A. *J. Am. Chem. Soc.* **2007**, *129*, 2504-2510.

(19)   Sacha, G. M.; Verdaguer, A.; Salmeron, M. *J. Phys. Chem. B* **2006**, *110*, 14870-14873.

(20)   Lu, W.; Kim, T.; Han, A.; Qiao, Y. *Mater. Chem. Phys.* **2012**, *133*, 259-262.

(21)   Daub, C. D.; Bratko, D.; Luzar, A. *Topics Curr. Chem.* **2012**, *307*, 155-180.

(22)   Vanzo, D.; Bratko, D.; Luzar, A. *J. Chem. Phys.* **2014**, *140*, 074710.

(23)   Gomez-Monivas, S.; Saenz, J. J.; Calleja, M.; Garcia, R. *Phys. Rev. Lett.* **2003**, *91*.056101.

(24)   Gupta, R.; Olivier, G. K.; Frechette, J. *Langmuir* **2010**, *26*, 11946-11950.

(25)   Yaminsky, V. V.; Yushchenko, V. S.; Amelina, E. A.; Shchukin, E. D. *J. Colloid Interface Sci.* **1983**, *96*, 301-306.

(26)   Lum, K.; Luzar, A. *Phys. Rev. E* **1997**, *56*, R6283-R6286.

(27)   Lum, K.; Chandler, D. *Int. J. Thermophys.* **1998**, *19*, 845-855.

(28)   Lum, K.; Chandler, D.; Weeks, J. D. *J. Phys. Chem. B* **1999**, *103*, 4570-4577.

(29)   Leung, K.; Luzar, A. *J. Chem. Phys.* **2000**, *113*, 5845-5852.

(30)   Bratko, D.; Curtis, R. A.; Blanch, H. W.; Prausnitz, J. M. *J. Chem. Phys.* **2001**, *115*, 3873-3877.

(31)   Leung, K.; Luzar, A.; Bratko, D. *Phys. Rev. Lett.* **2003**, *90*, 065502.

(32)   Luzar, A. *J. Phys. Chem. B* **2004**, *108*, 19859-19866.

(33)   Sharma, S.; Debenedetti, P. G. *J. Phys. Chem. B* **2013**, *116*, 13282-13289.

(34)   Evans, R. *J. Phys.: Condens. Matter* **1990**, *2*, 8989-9007.

(35)   Frank, H. S. *J. Chem Phys.* **1955**, *23*, 2023.

(36)   Luzar, A.; Bratko, D.; Blum, L. *J. Chem. Phys.* **1987**, *86*, 2955-2959.

(37)   Wallqvist, A.; Berne, B. J. *J. Phys. Chem.* **1995**, *99*, 2893-2899.
(38)   Truskett, T. M.; Debenedetti, P. G.; Torquato, S. *J. Chem. Phys.* **2001**, *114*, 2401-2418.
(39)   Chandler, D. *Nature* **2005**, *437*, 640-647.
(40)   Giovambattista, N.; Rossky, P. J.; Debenedetti, P. G. *Phys. Rev. E* **2006**, *73*, 041604.
(41)   Rasaiah, J. C.; Garde, S.; Hummer, G. *Annu. Rev. Phys. Chem.* **2008**, *59*, 713-740.
(42)   England, J. L.; Park, S.; Pande, V. S. *J. Chem. Phys.* **2008**, *128*, 044503.
(43)   Bratko, D.; Daub, C. D.; Luzar, A. *Phys. Chem. Chem. Phys.* **2008**, *10*, 6807-6813.
(44)   Bratko, D.; Daub, C. D.; Luzar, A. *Faraday Discuss.* **2009**, *141*, 55-66.
(45)   Lee, C. Y.; McCammon, J. A.; Rossky, P. J. *J. Chem. Phys.* **1984**, *80*, 4448-4455.
(46)   Luzar, A.; Svetina, S.; Zeks, B. *J. Chem. Phys.* **1985**, *82*, 5146-5154.
(47)   Lee, S. H.; Rossky, P. J. *J. Chem. Phys.* **1994**, *100*, 3334-3345.
(48)   Daub, C. D.; Bratko, D.; Leung, K.; Luzar, A. *J. Phys. Chem. C* **2007**, *111*, 505-509.
(49)   Daub, C. D.; Bratko, D.; Ali, T.; Luzar, A. *Phys. Rev. Lett.* **2009**, *103*, 207801.
(50)   von Domaros, M.; Bratko, D.; Kirchner, B.; Luzar, A. *J. Phys. Chem. C* **2013**, *117*, 4561-4567.
(51)   Bier, M.; Ibagon, I. *Phys. Rev. E* **2014**, *89*. 042409.
(52)   Yeo, L. Y.; Chang, H. C. *Phys. Rev. E* **2006**, *73*.
(53)   Vanzo, D.; Bratko, D.; Luzar, A. *J. Chem. Phys.* **2014**, *140*, 074710.
(54)   Frenkel, D.; Smit, B. *Understanding molecular simulation, from algorithms to applications*; Academic: San Diego, 2002.
(55)   Bolhuis, P. G.; Chandler, D. *J. Chem. Phys.* **2000**, *113*, 8154-8160.
(56)   Lei, Y. J.; Leng, Y. S. *Langmuir* **2012**, *28*, 3152-3158.
(57)   Choudhury, N.; Pettitt, B. M. *J. Am. Chem. Soc.* **2005**, *127*, 3556-3567.
(58)   Daub, C. D.; Bratko, D.; Luzar, A. *J. Phys. Chem. C* **2011**, *115*, 22393-22399.
(59)   Kalluri, R. K.; Biener, M. M.; Suss, M. E.; Merrill, M. D.; Stadermann, M.; Santiago, J. G.; Baumann, T. F.; Biener, J.; Striolo, A. *Phys. Chem. Chem. Phys.* **2012**, *15*, 2309-2320.
(60)   Kalluri, R. K.; Konatham, D.; Striolo, A. *J. Phys. Chem. C* **2011**, *115*, 13786-13795.
(61)   Berendsen, H. J. C.; Grigera, J. R.; Straatsma, T. P. *J. Phys. Chem.* **1987**, *91*, 6269-6271.
(62)   Vega, C.; Abascal, J. L. F.; Conde, M. M.; Aragones, J. L. *Faraday Discuss.* **2009**, *141*, 251-276.
(63)   Bako, I.; Ricci, M. A.; Debenedetti, P. G.; Rovere, M.; Havenith, M.; Coudert, F. X.; Luzar, A.; Klein, J.; Jungwirth, P.; Yamaguchi, T.; Lee, M.; Yarwood, J.; Michaelides, A.; Salmeron, M.; Feibelman, P.; Vega, C.; Patel, A.; Hodgson, A.; Finney, J.; Madden, P.; Uosaki, K.; Chen, J.; Jhe, W.; S. Perkin, S.; Halle, B.; Kim, S. J.; Bain, C.; Christenson, H.; Rao, M. L.; Held, G.; Lyashchenko, L.; von, K., R.; Van Der Niet, J.; Hooton, F.; Marques, M.; Wu, D. Y.; Johnson, S. *Faraday Discuss.* **2009**, *141*, 443-465.
(64)   Huang, D. M.; Geissler, P. L.; Chandler, D. *J. Phys. Chem. B* **2001**, *105*, 6704-6709.
(65)   Aragones, J. L.; MacDowell, L. G.; Siepmann, J. I.; Vega, C. *Phys. Rev. Lett.* **2011**, *107*, 155702.
(66)   Gereben, O.; Pusztai, L. *Chem. Phys. Lett.* **2008**, *507*, 80-83.
(67)   Agarwal, M.; Alam, M. P.; Chakravarty, C. *J. Phys. Chem. B* **2011**, *115*, 6935-6945.
(68)   Cheng, L. J.; Chang, H. C. *Biomicrofluidics* **2011**, *5*, 046502.
(69)   Vanzo, D.; Bratko, D.; Luzar, A. *J. Phys. Chem. C* **2012**, *116*, 15467-15473.
(70)   Sofo, J. O.; Chaudhari, A. S.; Barber, G. D. *Physical Review B* **2007**, *75*, 153401.

(71)   Elias, D. C.; Nair, R. R.; Mohiuddin, T. M. G.; Morozov, S. V.; Blake, P.; Halsall, M. P.; Ferrari, A. C.; Boukhvalov, D. W.; Katsnelson, M. I.; Geim, A. K.; Novoselov, K. S. *Science* **2009**, *323*, 610-613.

(72)   Lebegue, S.; Klintenberg, M.; Eriksson, O.; Katsnelson, M. I. *Phys. Rev. B* **2009**, *79*, 245117.

(73)   Fyta, M.; Netz, R. R. *J. Chem. Phys.* **2012**, *136*, 124103.

(74)   Yeh, I. C.; Berkowitz, M. L. *J. Chem. Phys.* **1999**, *111*, 3155-3162.

(75)   Vanzo, D.; Bratko, D.; Luzar, A. *J. Chem. Phys.* **2012**, *137*, 034707.

(76)   Raj, R.; Maroo, S. C.; Wang, E. N. *Nano Lett.* **2013**, *13*, 1509-1515.

(77)   Shih, C. J.; Strano, M. S.; Blankschtein, D. *Nature Materials* **2013**, *12*, 866-869.

(78)   Driskill, J.; Vanzo, D.; Bratko, D.; Luzar, A. *Wetting transparency of graphene in water, J. Chem. Phys. (2014) in press.*

(79)   Mugele, F.; Baret, J. C. *J. Phys.: Condens. Matter* **2005**, *17*, R705-R774.

(80)   Shapiro, B.; Moon, H.; Garrell, R. L.; Kim, C. J. *J. Appl. Phys.* **2003**, *93*, 5794-5811.

(81)   Dzubiella, J.; Hansen, J. P. *J. Chem. Phys.* **2004**, *121*, 5514-5530.

(82)   Kolafa, J.; Viererblova, L. *Journal of Chemical Theory and Computation* **2014**, *10*, 1468-1476.

(83)   Ballenegger, V.; Hansen, J. P. *J. Chem. Phys.* **2005**, *122*.

(84)   Bonthuis, D. J.; Gekle, S.; Netz, R. R. *Langmuir* **2012**, *28*, 7679-7694.

(85)   Yeh, I. C.; Berkowitz, M. L. *J. Chem. Phys.* **1999**, *110*, 7935-7942.

(86)   Philippsen, A.; Im, W. P.; Engel, A.; Schirmer, T.; Roux, B.; Muller, D. J. *Biophys. J.* **2002**, *82*, 1667-1676.

(87)   Song, C. R.; Wang, P. S. *Rev. Sci. Instrum.* **2010**, *81*, 054702.

(88)   Sutmann, G. *J. Electroanal. Chem.* **1998**, *450*, 289-302.

(89)   Stuve, E. M. *Chem. Phys. Lett.* **2012**, *519-20*, 1-17.

(90)   Saitta, M. A.; Saija, F.; Giaquinta, P. *Phys. Rev. Lett.* **2012,** 108, 207801.

(91)   Karnik, R.; Fan, R.; Yue, M.; Li, D. Y.; Yang, P. D.; Majumdar, A. *Nano Lett.* **2005**, *5*, 943-948.

(92)   Jorgensen, W. L.; Madura, J. D.; Swenson, C. J. *J. Am. Chem. Soc.* **1984**, *106*, 6638-6646.

Table 1: Lennard-Jones parameters and charges used for the simulation of butyl functionalized graphane surfaces and sodium chloride ions. Hydrocarbon groups are described by the OPLS-UA (united atom) force field. [92] and the values for ions are taken from Fyta and Netz[73]

Atom	σ [Å]	ε[kcal mol^{-1}]	q [e$_o$]
C, RCH_3 (123°)	3.905	0.175	0.00
C, RCH_3 (128°)	3.905	0.100	0.00
C, R_2CH_2	3.905	0.118	0.00
C, R_3CH	3.850	0.080	0.00
C, R_4C	3.800	0.050	0.00
Na^+	2.583	0.100	1.00
Cl^-	4.40	0.100	-1.00
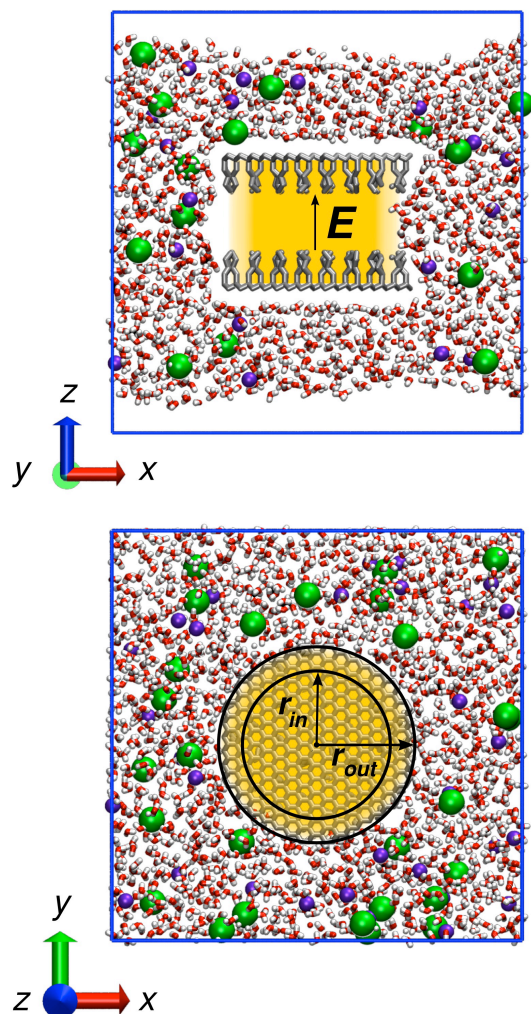
Figure 1 Simulation setup consisting of a rectangular box filled by electrolyte solution. Top: side view of the system, showing the empty hydrophobic confinement between a pair of disk-like platelets made of butylated graphane. Aqueous phase pervading the simulation box is flanked by vapor pockets adjacent to purely repulsive walls at the bottom and top boundaries of the box. Yellow color denotes the region subject to weak electric field. When the field intensifies, the region is filled by the solution. Bottom: top view of the box showing the regions of uniform ($r<r_{in}$) and fading electric field ($r_{in}<r<r_{out}$). Thin slices of the system are shown for better visualization.
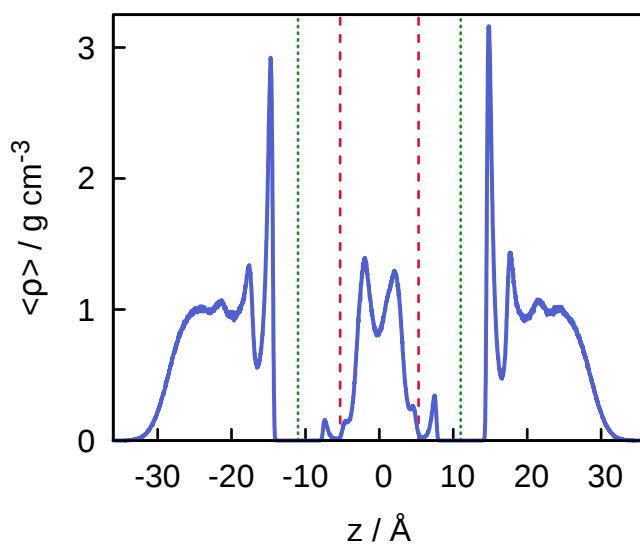
Figure 2 Density profiles of water (blue line) inside the central portion of the simulated system. Vertical lines denote the positions of graphane backbones (dashed green) and terminal methyl groups of butyl functionalizing chains (dashed red lines). The difference in peak heights at the inner and outer confinement surfaces reflect different contact angles, ~128° on the inner (butylated) and 73° on the outer (bare graphane) side. The profiles reveal minute penetration of water into the butyl brush. The asymmetry of the peaks is associated with electric field and polarization of water inside the pore (D_z=0.031 Cm^{-2}). The confinement spontaneously evacuates upon cessation of the field.
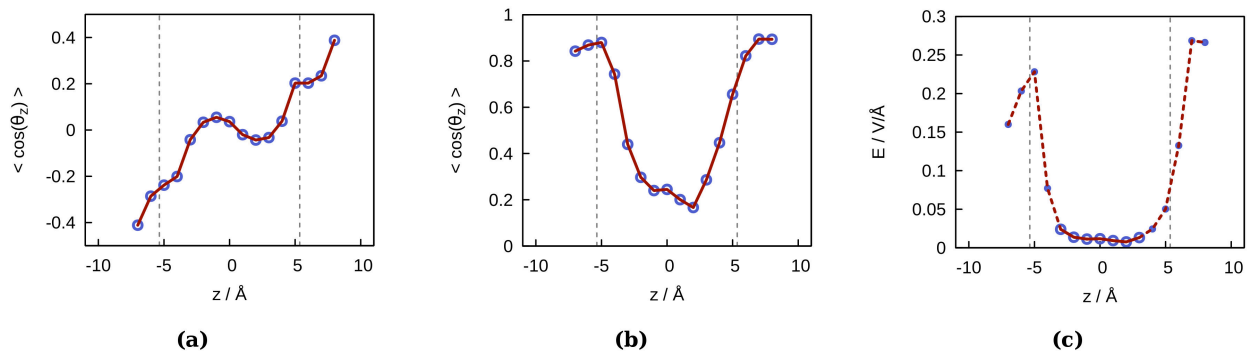
Figure 3 Polarization of water, measured in terms of the average angle between water dipoles and wall normal (z axis) inside 11 Å aqueous confinement: (a) spontaneous polarization in the absence of electric field, (b) displacement field $D_z=0.031$ Cm^{-2} (c) electric field profile inside the confined aqueous slab.
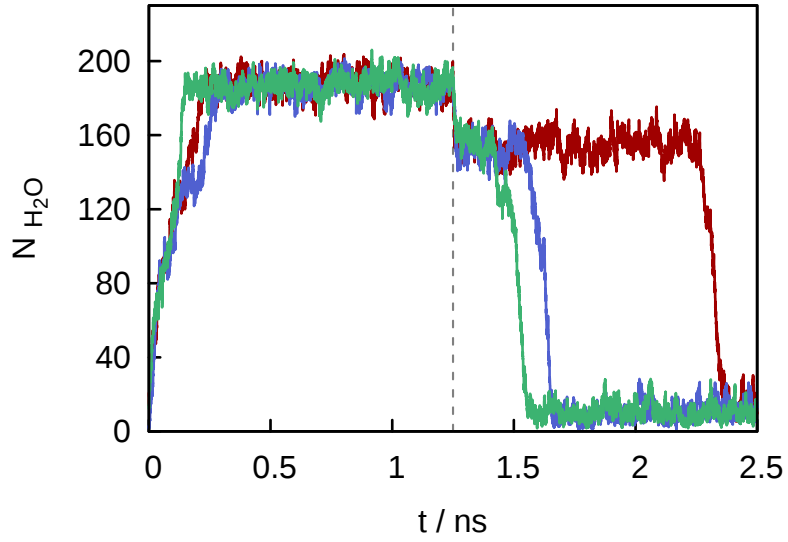
**Figure 4** Time dependence of the number of water molecules, N_{H2O}, inside a nanopore with radius r_{out}=17Å, r_{in}=13Å, and h=11Å. Time origin corresponds to the imposition of the field (D_z=0.031 Cm^{-2}). The field is switched off at t=1.25 ns. Different colors describe three independent runs at identical conditions.
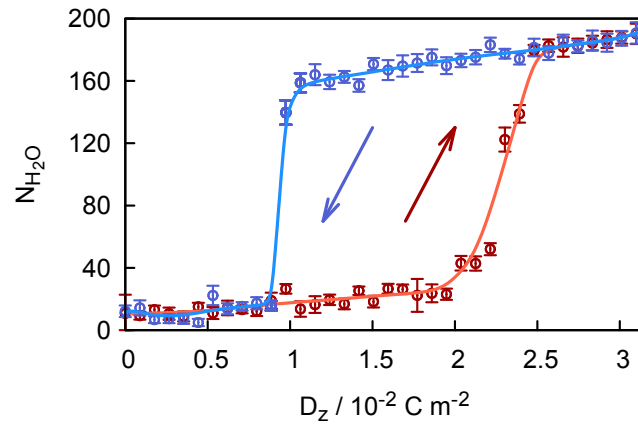
**Figure 5**. Typical density evolution, measured in terms of the number of water molecules, N_{H2O}, inside a nanopore with radius r_{out}=17Å, r_{in}=13Å, and h=11Å, as a function of monotonically increasing (red curve) or decreasing (blue curve) electric displacement field D_z. The rate of field change, $dD_z/dt = \pm 9 \cdot 10^{-3}$ Cm^{-2}s^{-1}.
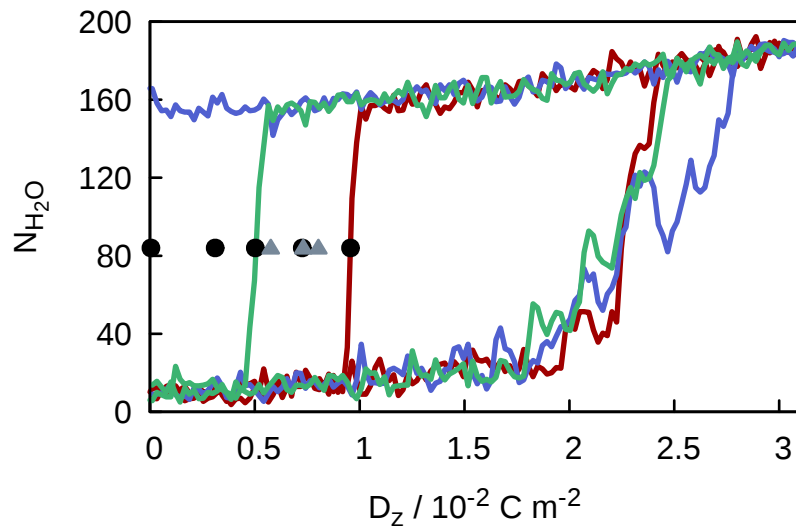
Figure 6 A survey of eleven infiltration-expulsion cycles in neat water, described in terms of the number of water molecules, N_{H2O}, in the nanopore (r_{out}=17Å, r_{in}=13Å, and h=11Å) as a function of electric displacement field D_z. Three cycles (red, blue and green) are shown in full. As the shape of the cycles is similar in all cases, for the remaining eight cycles, we merely mark the positions of abrupt expulsion. Red, blue and green curves, and solid black circles correspond to the rate of field change dD_z/dt of $\pm 9 \cdot 10^{-3}$ Cm^{-2}s^{-1}. The three grey triangles were obtained at slower field decrease rate of -4.5$\cdot 10^{-3}$ Cm^{-2}s^{-1}. Infiltration branches determined at the slower field increase showed no appreciable difference from those obtained at twice higher rate. One of the expulsion branches (blue) was completed at the time outside the plotted range.
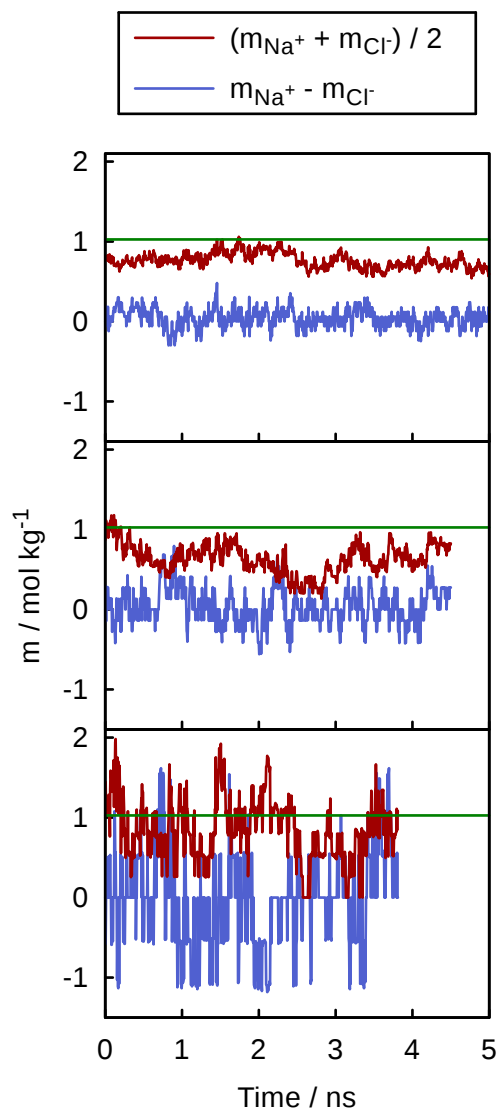
Figure 7 Time dependence of ion molalities: $(m_{Na^+}+m_{Cl^-})/2$ (red), and $(m_{Na^+}-m_{Cl^-})$ as a measure of deviation from neutrality inside the confinement core ($r \leq r_{in}$ (blue) with wall separation h=19 Å and radius r_{out}=32 Å. The field corresponds to D_z=0.031 Cm^{-2}. r_{in} =24 Å (top), 16 Å (middle) or 8 Å (bottom graph). Average electrolyte concentration in the confinement core is around 30% below the bulk value of 1.027 mol kg^{-1}(green line).
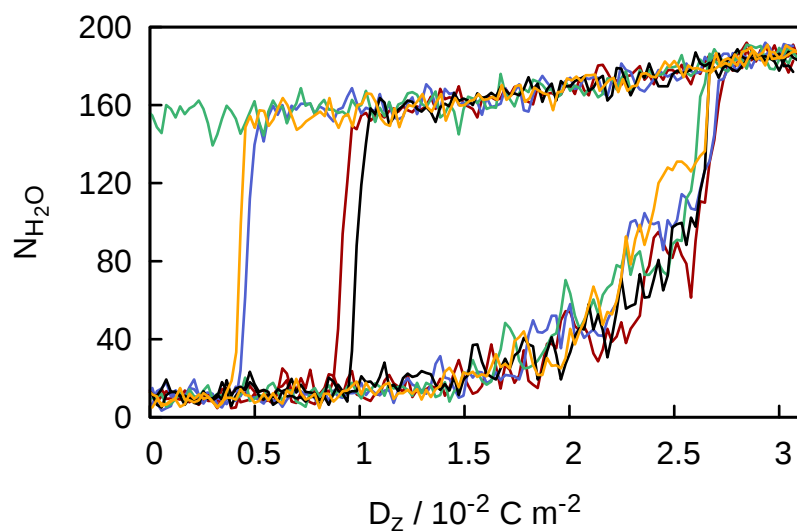
Figure 8 Infiltration (lower) and expulsion (upper) branches in 1.027 mol kg^{-1} NaCl solution, described by plotting the number of water molecules, N_{H2O}, inside a nanopore with radius r_{out}=17Å, r_{in}=13Å, and h=11Å, in five independent cycles at identical conditions. The rate of field increase and subsequent decrease dD_z/dt was ±9·10^{-3} Cm^{-2}s^{-1}.
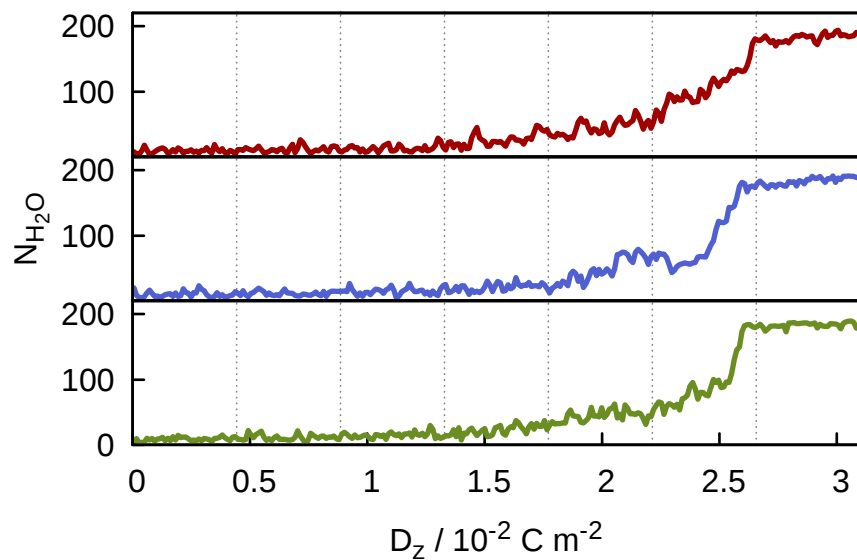
Figure 9. The infiltration branches in 1.027 mol kg^{-1} NaCl showing the number of water molecules, N_{H2O}, inside a nanopore with radius r_{out}=17Å, r_{in}=13Å, and h=11Å, as a function of monotonically increasing electric displacement field D_z. The rate of field change (dD_z/dt) was 4.5·10^{-3} Cm^{-2}s^{-1}. Different colors correspond to independent runs at identical conditions.
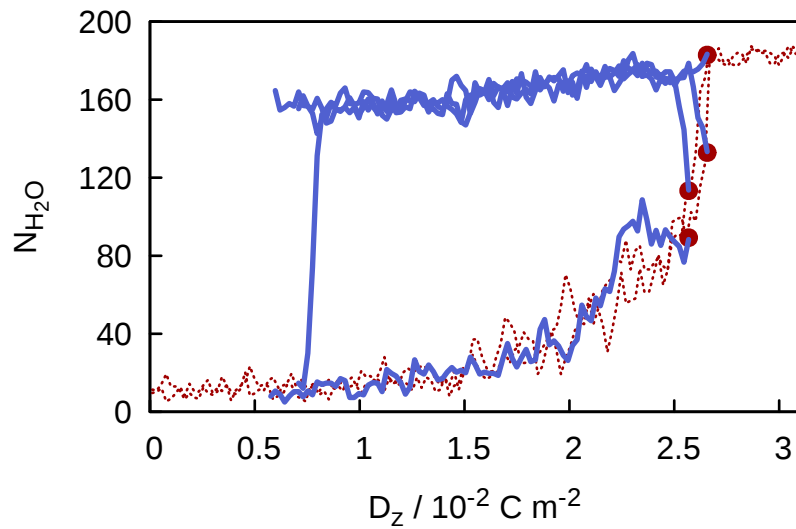
Figure 10 Density evolution (quantified in terms of the number of water molecules, N_{H2O}) in four backward runs (decreasing field, $dD_z/dt = - 9 \cdot 10^{-3}$ $Cm^{-2}s^{-1}$) inside a nanopore with radius r_{out}=17Å, r_{in}=13Å, and h=11Å. The runs were initiated at four configurations (solid circles) taken from previous infiltration (increasing field) branches (dashed red). The data are indicative of a shallow barrier to intrusion at about 50% infiltration.